Ceramics International 44 (2018) 8176–8183

Contents lists available at ScienceDirect

Ceramics International

journal homepage: www.elsevier.com/locate/ceramint

In-situ stress gradient evolution and texture-dependent fracture of brittle ceramic thin films under external load

Yeting Xi[a], Yanyun Bai[a], Kewei Gao[a], Xiaolu Pang[a,*], Huisheng Yang[a], Luchun Yan[a], Alex A. Volinsky[b]

[a] School of Materials Science and Engineering, University of Science and Technology Beijing, Beijing 100083, PR China
[b] Department of Mechanical Engineering, University of South Florida, Tampa, FL 33620, USA

ARTICLE INFO

Keywords:
In-situ
Stress gradient
Ceramic thin films
Texture transition
Fracture toughness
Modeling

ABSTRACT

Brittle ceramic thin films failure problems induced by film stress during service have been recently getting more attention. Thus, it is crucial to know the stress to understand correlated film fracture. In this work, in-situ stress gradient evolution during cracking of TiN films under external load was investigated by grazing-incidence X-ray diffraction using the optimized $\cos^2\alpha \sin^2\psi$ method. Counterintuitively, cross-sectional scanning electron microscopy clearly demonstrated that cracks initiated in the middle of the film thickness and propagated to the surface and/or the interface with increased load. Eventually, film through-thickness crack and even delamination occurred. Preferred orientation evolution and texture transition along the film cross-section were characterized by selected area electron diffraction in transmission electron microscopy and the Kikuchi diffraction analysis. Thermodynamics modeling revealed that system energy was the driving force for dominant texture transition. The texture-dependent film fracture toughness accounts for the film cracking behavior. A model of fracture toughness is proposed to consider and evaluate the effect of the preferred orientation. The fracture toughness in the middle of the film, where the texture transition zone is located, is smaller than at the surface or the interface. Consequently, the texture transition zone of the film becomes the crack initiation point, which finally leads to the whole film-substrate system failure. Consequently, the texture transition zone of the film becomes the crack initiation point, which finally leads to the whole film-substrate system failure.

1. Introduction

With the demand of prolonging lifetime and improving performance of materials, thin hard films are widely used in various industrial applications [1]. Hard thin films can reduce friction, enhance wear [2] and oxidation resistance [3,4], along with anti-corrosion properties [5] of substrates. However, failures, including cracking [6], delamination or spallation [7,8], prevent thin films or coatings device integration [9]. Additionally, residual stress is important, since it can affect many mechanical properties of thin films [10,11], such as adhesion, fracture toughness, elastic modulus and hardness. In fact, quite a lot of film failures during their service life are induced by film stress. Consequently, it is crucial to know the film stress and understand how it correlates with film failures during service.

Stress gradient along the film thickness is quite important for film failure because it is closely related to crack initiation and propagation. Extensive studies of thin film stresses have been conducted in the past [12–17]. However, previous research paid more attention to films fracture behavior under different deposition conditions rather than the in-situ stress gradient evolution. Magnetron-sputtered CrN thin films with 100 nm to 3 μm thickness were investigated, and the residual stress was reported as a function of film thickness. The film exhibited maximum compressive stress in the 100 nm CrN layer, which rapidly decreased with film thickness, finally reaching a plateau value [12]. TiN thin film on single crystal silicon substrates was investigated. X-ray diffraction (XRD) techniques were used to characterize residual stress in thin films with different thickness ranging from 85 nm to 2.5 μm. The stress in the films decreased with the film thickness [13]. The existence of the film stress gradient was confirmed by pencil-beam X-ray nano-diffraction, reporting higher stress at the film surface [14]. Residual stresses in different Ti-TiN multilayers were investigated and their effects on adhesion were studied using experiments combined with simulations. In each layer of the coatings, the maximum residual stresses were at the layer-to-layer interfaces, and the highest stress value of the entire coating was at the coating-to-substrate interface [15]. Renzelli et al. [16] studied the residual stress gradient in the Cr/CrN multilayer

* Corresponding author.
E-mail address: pangxl@mater.ustb.edu.cn (X. Pang).

https://doi.org/10.1016/j.ceramint.2018.01.265
Received 4 January 2018; Received in revised form 29 January 2018; Accepted 31 January 2018
Available online 02 February 2018

coatings, and found that the interfacial film stress is larger than at the surface or the middle part of the film thickness. This means that the stress concentration takes place at the film-substrate interface. They also found that the stress gradient may change according to different designs of the layers. Additionally, the hole-drilling method was used for the stress gradient characterization of multilayer films. Besides, the method of wet chemical etching was also employed to obtain film stress gradient in another research report about the residual stress in TiN thin films with the film thickness ranging from 20 nm to 1.9 μm [17]. Film stress was measured using the substrate curvature method and the average film stress was compressive and higher stress was present in thinner films. However, the abovementioned methods are destructive, thus affecting the accuracy of the results. According to the previous research reports, stress gradient exists. However, it is not enough to interpret thin film failure problems in actual applications because of a lack of understanding of the stress gradient evolution mechanism. To reveal the film cracking behavior during the failure process, more information about the stress gradient is needed, especially in-situ cracking processes of the films.

Fracture toughness represents the ability of a material to resist crack propagation upon loading [18]. Fracture toughness is an important property of brittle materials, including hard ceramics thin films and coatings, and many methods for measuring the mode-I fracture toughness have been developed [19]. Basically, these methods can be summarized into two categories, i.e. the stress-based approach and the energy-based approach [20]. The stress-based approach includes bending or buckling, indentation and scratch tests [21–23]. However, these measurement methods inevitably initiate a crack, since no pre-crack exists to start with [24]. Consequently, the accuracy of these methods cannot be assured. Therefore, energy-based approach is more viable. The main advantages of the energy-based methods are no need for special preparation and externally applied load [25]. This approach is more reliable for thin films [26–28].

To reveal the real time film cracking behavior, more information about the stress gradient is needed. The emphasis of this work is on in-situ film stress gradient evolution during external loading, film failure behavior and correlated mechanisms. Based on the growth mechanisms and fracture toughness modeling, stress gradient evolution and film cracking behavior under different circumstances can be illustrated.

2. Experimental procedure and theoretical basis

2.1. Materials preparation

TiN thin film was selected in this study as representative brittle ceramic film. The film was deposited by unbiased reactive RF-pulsed magnetron sputtering on polished AISI 304 stainless steel (304 SS) substrates. The size of the substrates was 20 mm × 15 mm × 2 mm. Before deposition, the substrates were cleaned in acetone for 10 min in ultrasonic cleaner and Ar^+ ion bombardment with 100 W power for 20 min was employed to activate specimens' surface and remove surface contamination. The purity of Ti target was 99.995% and the base pressure was better than 4.5×10^{-3} Pa. To improve adhesion between the film and the substrate, Ti metal interlayer with the thickness of about 100 nm was deposited first. The sputtering power of the Ti target was 300 W. The substrate temperature was kept at 300 °C. The working pressure was kept at 2.9×10^{-1} Pa. After deposition, thin films underwent natural cooling to room temperature in the vacuum chamber.

2.2. Film characterization

Cross-sectional microstructure and cracking behavior of the TiN thin films were observed by field emission scanning electron microscopy (FESEM, Supra 55, Zeiss, Germany). Phase crystallographic structure of the films was identified using X-ray diffractometry (Cu target, SmartLab, Rigaku, Japan) with 40 kV and 150 mA. The wavelength of Cu $K_{\alpha 1}$ radiation was 1.5406 Å. The Young's modulus of TiN thin films was measured by nanoindentation (TriboIndenter, Hysitron, USA). The indentation depth was within 10% of the film thickness to avoid the substrate effects [29] and a constant loading rate of 200 μN/s was used. Preferred orientation of the films along the film cross-section was determined by selected area electron diffraction (SEAD) mode in field-emission transmission electron microscope (TEM, JEOL 2100-F, Japan). Transmission Kikuchi diffraction analysis (TKD, or transmission electron back-scattered diffraction, t-EBSD, Bruker, Germany) was utilized to obtain detailed film growth information. Focused ion beam (FIB, Tescan, Czech Republic) was used to prepare thin film cross-section samples.

2.3. Stress gradient evolution

Film stress measurements were accomplished by GIXRD using thin film accessory and a homemade optimized sample stage. Grazing incidence diffraction geometry has several advantages, such as limiting the beam penetration depth, increasing the diffraction volume of the films, and avoiding diffraction reflection from the substrate. Parallel beam optics and side-inclination method were utilized. This technique allows obtaining in-situ stress gradient evolution in thin films more accurately and non-destructively [30]. The $\cos^2 \alpha \sin^2 \psi$ method was used and the bi-axial film stress was determined from measuring the lattice spacing d_{hkl} at several inclination angles ψ [31]. Changing the grazing incidence angle provides depth-dependent residual stress in thin films, allowing to obtain the stress gradient [32].

Schematic diagrams of the three-point bending fixture with a sample in Fig. 1(a), and Fig. 1(b) show the samples with and without bending. To ensure in-situ stress gradient measurement accuracy, the sample was held in the same position and height during the whole X-ray measurement process. The homemade bending fixture was rigidly attached to the sample holder. The sample steel disc with a groove was attached to the bending fixture, shown in Fig. 1(c), and placed in the middle of X-ray incident beam. The appropriate sample height was set to obtain maximum X-ray signal intensity. The stress gradient of the as-deposited film was characterized first. Then a certain external load/strain was applied to the sample, controlled by a strain gauge (program-controlled static resistance strain gauge, BZ2205C). Each time after the external load was applied, stress gradient measurement was performed.

Residual stress in thin film was characterized based on the $\cos^2 \alpha \sin^2 \psi$ method, which utilizes asymmetric diffraction geometry. The basic principle of the method is consistent with the traditional $\sin^2\psi$ method, which means the bi-axial residual stress of thin film is determined from measuring the lattice spacing d_{hkl} at several inclination angles ψ. In a single test, a fixed (*hkl*) Bragg reflection plane is selected. The bi-axial strain in $\cos^2 \alpha \sin^2 \psi$ method is given by [31]:

$$\frac{d_{\alpha\psi} - d_0}{d_0} = \frac{1+\nu}{E}\sigma cos^2\alpha sin^2\psi + \frac{1+\nu}{E}\sigma sin^2\alpha - \frac{2\nu}{E}\sigma \quad (1)$$

In Eq. (1), $d_{\alpha\psi}$ represents the lattice spacing gained from the (*hkl*) planes and d_0 represents the lattice spacing of the stress-free sample. Here, E is the Young's modulus and ν is the Poisson's ratio. From the linear fitting results between strain $\frac{d_{\alpha\psi} - d_0}{d_0}$ and $\cos^2\alpha \quad \sin^2\psi$, one can get the slope $\frac{1+\nu}{E}\sigma$, which is the basis of residual stress calculation. Fig. 2 shows the schematic diagram of grazing incidence X-ray diffractometry, and the instrumental angles are as follows: θ: Bragg's angle; γ: X-ray beam grazing incidence angle; α: angle between the sample surface, the diffraction plane and ψ: the inclination angle of the sample surface. Apparently, $\alpha = \theta - \gamma$, where θ is the Bragg's angle of the (*hkl*) planes. Changing the grazing incidence angle provides depth-dependent residual stress in thin films, allowing to obtain the stress gradient. The penetration depth is determined as [32]:

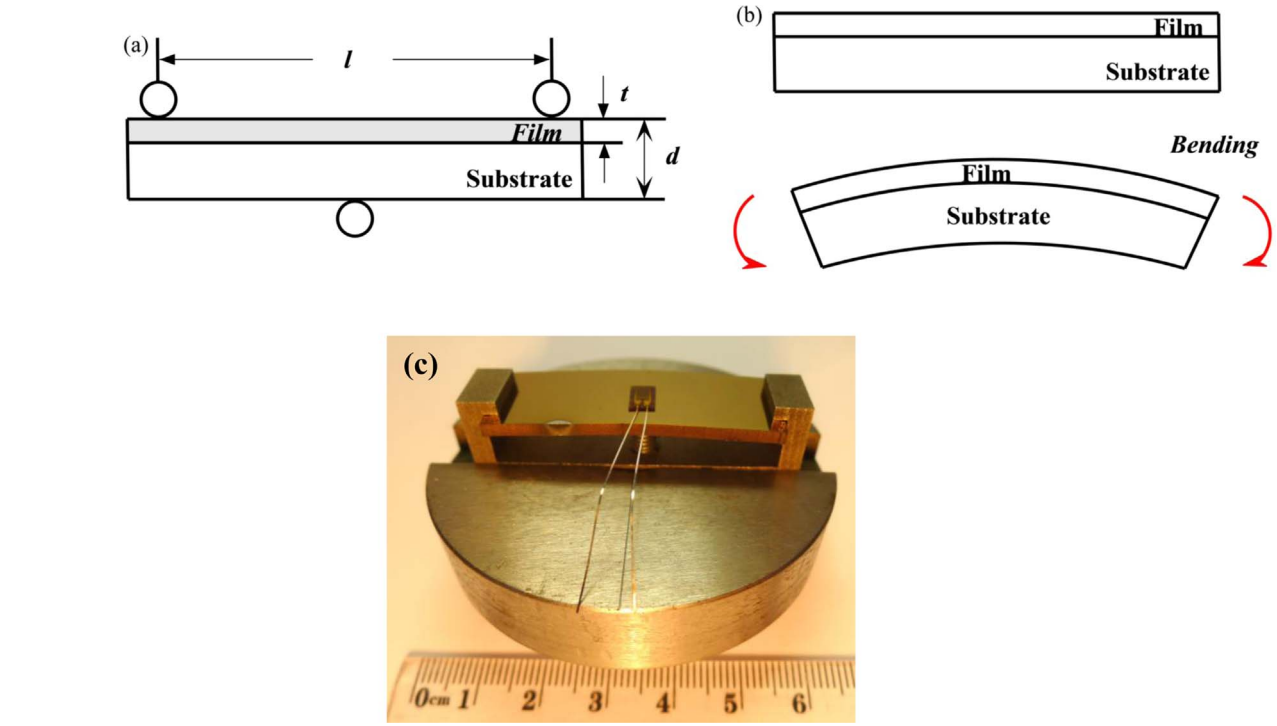

Fig. 1. (a) Schematic diagrams of bending fixture with a sample; (b) Schematic diagrams of sample without bending and under bending; (c) XRD bending fixture with the sample and the strain gauge attached to the TiN film surface.

$$\tau = \frac{\cos\Psi\,(sin^2\,\theta - sin^2\,\alpha)}{2\mu\sin\theta\cos\alpha} \quad (2)$$

In Eq. (2), Ψ is the inclination angle; θ is the Bragg's angle; α is the angle between the sample surface and the diffraction plane, and $\alpha = \theta - \gamma$; μ is the liner absorption coefficient of the irradiated material for the used X-ray wavelength. For a given thin film sample and corresponding diffraction parameters, film thickness, absorption coefficient, Poisson's ratio and Young's modulus are constants. By applying suitable grazing incidence angle, the stress gradient can be measured.

2.4. Thermodynamics modeling

Total energy of the system is the dominant factor of the polycrystalline thin films during growth. The energy of the orientations were simulated and calculated based on the first principles. In this work, surface energy calculations were executed using the CASTEP module of Materials Studio 8.0 (Accelry Inc.). Generalized gradient approximation (GGA) by the Perdew-Bruker-Ernzerhof method (PBE) was applied to calculate the exchange-correlation potential. During the calculation process, the cutoff energy was 350 eV, the total energy tolerance was 5×10^{-7} eV/atom, and the *k*-point was $10 \times 10 \times 1$.

2.5. Fracture toughness evaluation

The internal energy induced cracking (IEIC) method [33] was used to evaluate the fracture toughness of the thin films. This method is an energy-based approach and the principle lies in the energy difference.

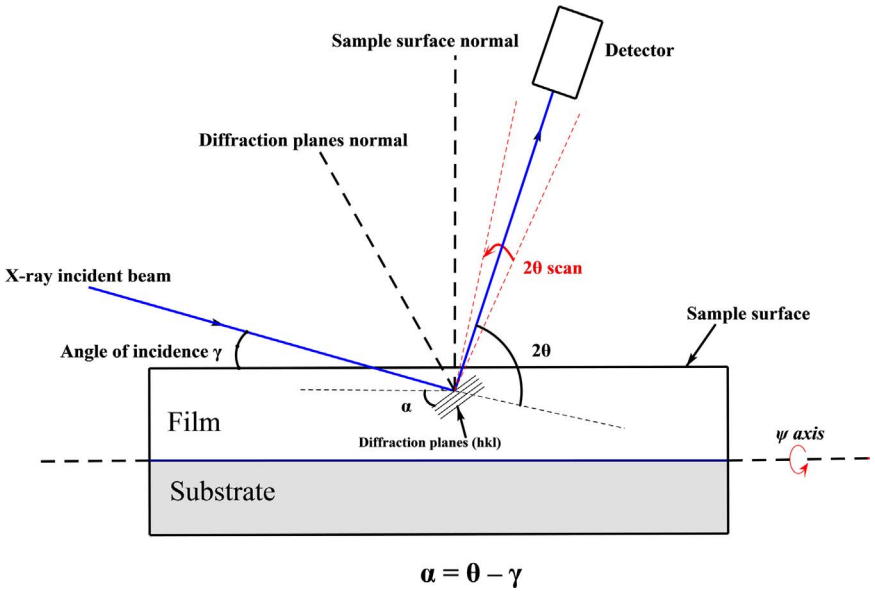

Fig. 2. Schematic diagram of grazing incidence X-ray diffractometry (GIXRD).

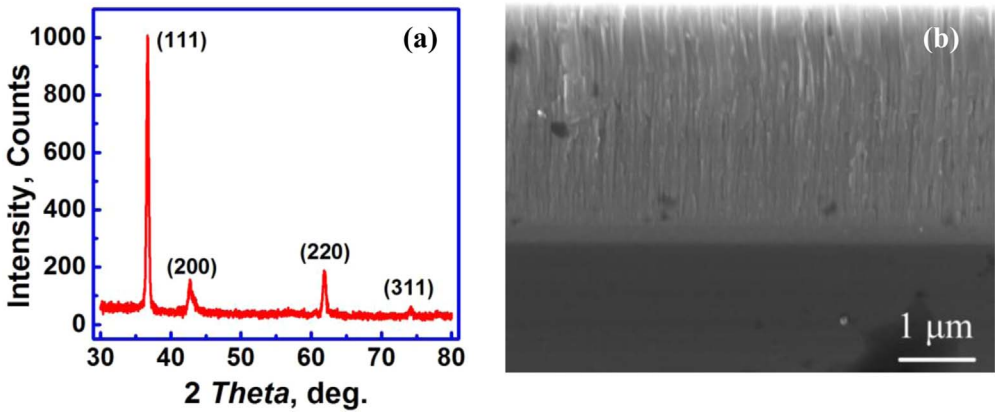

Fig. 3. (a) GIXRD spectra of 2.9 μm TiN thin film; (b) SEM cross-section morphology of TiN thin film.

The energy release rate is calculated based on the energy difference, which is considered to be responsible for film fracture. Fracture toughness can be calculated once the energy release rate is obtained [20].

3. Results and discussion

3.1. Film crystal structure and microstructure

To identify the phase and crystal structure of the TiN films, GIXRD spectra are shown in Fig. 3(a). The grazing incidence angle is fixed at 2°. Taking the standard reference sample into account (JCPDS 38-1420), the films can be assigned to the TiN face-centered cubic (FCC) structure. The diffraction peaks at 2 *theta* = 37°, 42.8°, 62.3° and 74.4° correspond to (111), (200), (220) and (311) planes of TiN, respectively.

Cross-sectional morphology of the sputtered TiN films was characterized by SEM. Fig. 3(b) shows representative microstructure of the film, where typical columnar microstructure perpendicular to the film surface can be seen. An average surface roughness measured by Veeco Dektak 150 stylus profilometer was approximately 4.5 nm. The thickness of TiN films is about 2.9 μm. The width of the columnar grains is in several tens of nanometers, and the width gets larger with the distance from the film-substrate interface to the film surface, indicating nanoscale grain size.

3.2. Film mechanical properties

Young's modulus of the TiN films was measured by nanoindentation. The indentation depth was within 10% of the film thickness, which was between 200 nm and 290 nm, to avoid the substrate effect. Five tests were made to ensure results reliability. The measurement results were 314.18 GPa, 300.56 GPa, 311.81 GPa, 301.75 GPa and 314.73 GPa, respectively. Every value is an average of five indentation tests. As a consequence, the average value of the TiN thin films Young's modulus was 308.61 GPa.

3.3. In-situ stress gradient evolution

The stress gradient evolution of the film under externally applied strain is shown in Fig. 4. In this study, TiN (220) plane was chosen for the stress measurements in the 61–64° 2θ range. Eight inclination angles were used, ranging from 0° to 45° (0°, 15°, 20°, 25°, 30°, 35°, 40° and 45°). Parameters relevant to X-ray residual stress measurements are listed in Table 1. The film cross-section was divided into three approximate areas along its thickness, i.e. surface, middle and interface regions. In this study, they are defined as region I, II and III, respectively. According to Eq. (2), the penetration depth at 2.5°, 9° and 19.5° incident angles was about 500 nm, 1500 nm and 2500 nm, respectively,

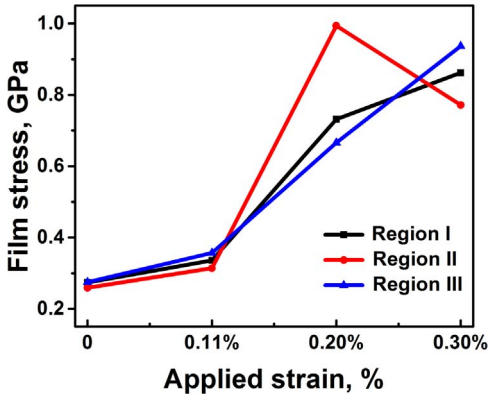

Fig. 4. In-situ film stress evolution under externally applied strain.

Table 1
Parameters used in residual stress measurements by XRD.

Material	TiN (JCPDS#38-1420)
Wavelength, λ	Cu $K_{\alpha 1}$ (1.5406 Å)
Linear absorption coefficient, μ	879 cm^{-1}
Reflection planes, (*hkl*)	(220)
Diffraction angle, 2θ	61.81°
Young's modulus, *E*	308.61 GPa
Poisson ratio, ν	0.21
Lattice spacing, d_0	1.4997 Å

which are representative of surface, middle and interface regions of the film. In Fig. 4, the three regions show different response to externally applied strain. The loading process can be divided into three stages. At the beginning, when the externally applied strain was varied from 0% to 0.1%, the whole film had almost the same stress along its thickness, which increased with the strain at the same rate, demonstrating no stress gradient. This is apparent from the same stress-strain slope between 0% and 0.1% strain for all regions in Fig. 4. The second loading stage is between 0.1% and 0.2% strain. During this stage, film stresses in all regions increase rapidly and film stress in region II increases at a faster rate than in region I and III. When the applied strain is between 0.2% and 0.3%, the stress in region I and III continues to increase. However, the film stress in region II rapidly decreases, pointing to the exact location of film stress relief.

It is worth noticing that the stress values in region I and III are lower than the maximum stress value in region II during the whole loading process. The results further demonstrate that different film regions have different mechanical properties. Specifically, the middle region is more vulnerable to crack initiation in thin hard films, which finally leads to the whole film-substrate system failure.

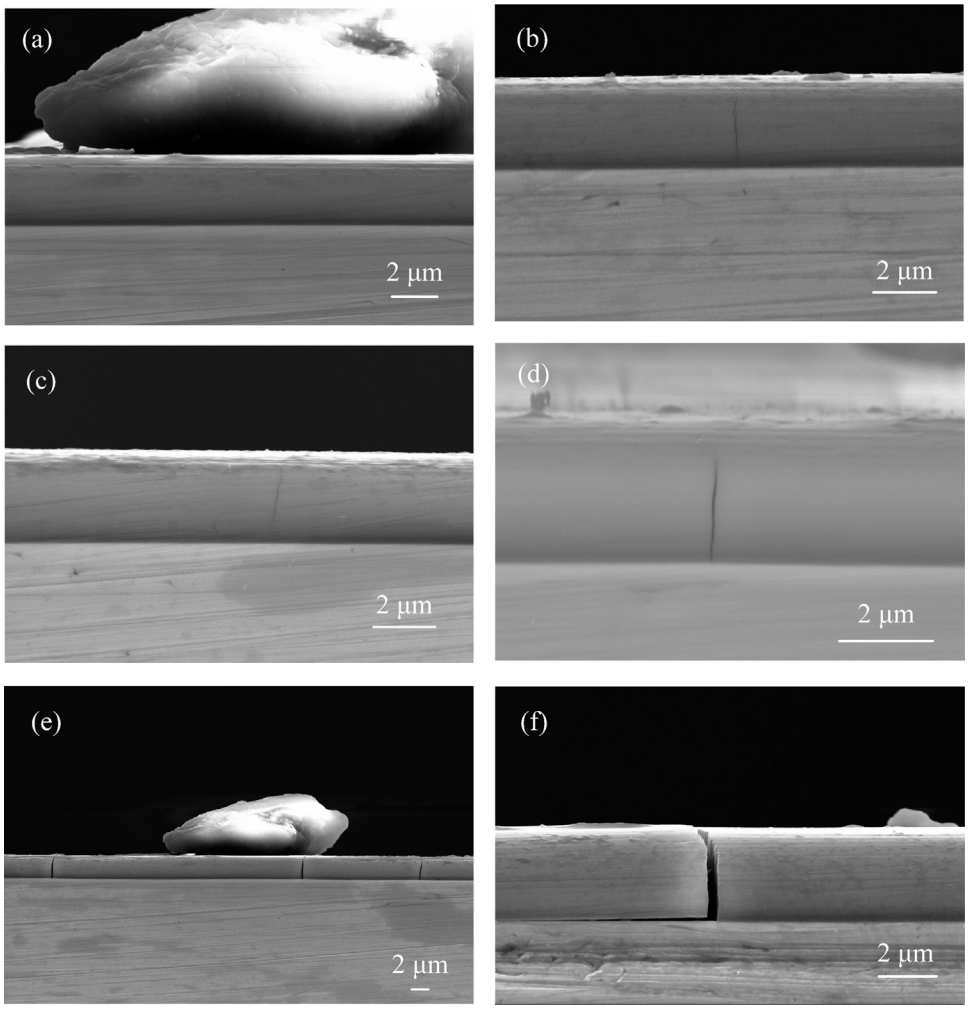

Fig. 5. Cross-section cracking morphologies of films under different strain: (a) 0; (b) 0.22%; (c) 0.26%; (d) 0.26%; (e) 0.4%;(f) 0.5%.

3.4. Film cracking behavior

Film cracking behavior is shown in Fig. 5. The cross-sectional view of TiN thin films was investigated under gradually increased external strain/stress. The external strain was gradually increased from 0% to 0.5%. Each time after the external load was applied, the sample was observed in SEM under load in the fixture. Then additional external load was applied based on the previous value to keep the observed zone consistent. Cross-section cracking morphology of films under gradually increasing load/strain is shown in Fig. 5. Comparison of Fig. 5(a) and 5(e) clearly shows that under 0.5% applied strain, the cracks in TiN thin film were all through-thickness cracks, while the thin film was still intact without any strain. In Fig. 5(b), 5(c), and 5(d), no through-thickness cracks can be found under the increasingly applied strain of 0.22%, 0.26% and 0.26%, respectively. All cracks were mainly present in the middle of the film thickness. Only a small part of the crack propagated into the other two regions, but had not reached the surface or the interface yet. Besides, Fig. 5(c) shows that a crack was mainly in the middle and propagated towards the surface, but not into the interface. Additionally, Fig. 5(d) shows that a crack in the middle region, propagated towards the interface, rather than the film surface.

Consequently, these figures indicate the crack initiation occurs in the middle of the film thickness, and the crack propagated gradually to the surface or the interface with the external load reaching a certain value. Moreover, when the applied strain was beyond 0.3%, through-thickness cracks were observed. As seen in Fig. 5(e) and 5(f), through-thickness cracks and even film delamination occurred when the applied strain was 0.4% and 0.5%, respectively. This phenomenon agreed with the film stress gradient evolution. Based on the experimental evidence of stress gradient and SEM results, it is reasonable to attribute film failure to the through-thickness cracks, which initiated from the middle of the thin film and propagated into the surface and/or interface when the externally applied strain exceeded a critical value.

3.5. Film texture transition zone

To obtain the film preferred orientation information in region II, TEM was employed. The preparation of the cross-sectional electron transparent films was accomplished by FIB, which is relatively rapid compared to conventional techniques [34]. The FIB cross-section specimen with uniformly thin area was prepared. The middle region of the cross-section sample was characterized using the SEAD mode. Typical electron diffraction pattern from the region II of TiN thin film cross-section is shown in Fig. 6(a). Randomly distributed spots are seen, marked as A, B and C. This result indicates polycrystalline character of the film. Moreover, spots A, B and C in the diffraction pattern can be indexed to TiN (111), (200) and (220) reflections, respectively. This proves the existence of mixed orientations in the middle region of the film.

As is known, the electron backscatter diffraction (EBSD) test would be ideal to get growth information of materials. However, EBSD is hard to perform for the thin film materials whose grain size is relatively small compared to the bulk materials. In this work, the TKD (or the t-EBSD) was utilized to overcome this problem. The preparation of the cross-sectional sample of the film was also accomplished by FIB. The test mainly focused on the middle of region II of the film. The result is

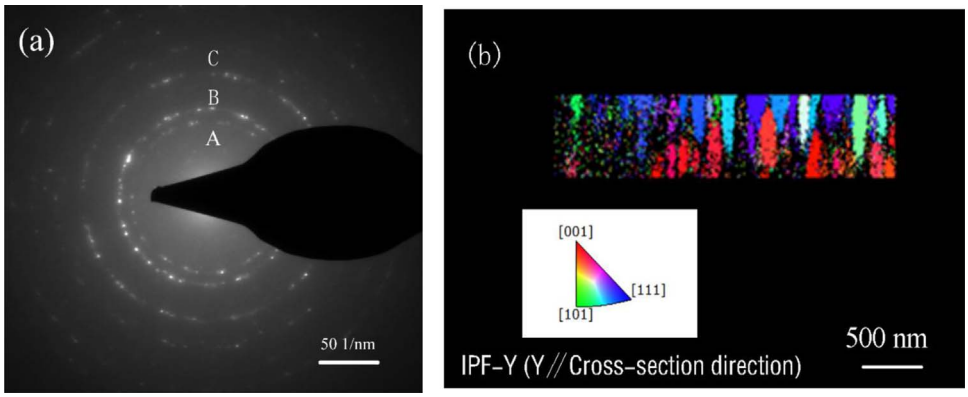

Fig. 6. (a) SAED pattern from the middle of cross-sectional of the TiN film by TEM; (b) Orientation map of the middle of TiN film cross-section by TKD.

given in Fig. 6(b), which shows the orientation map (inverse pole figure Y-direction coloring scheme, where Y is parallel to the cross-section direction of the film). In the middle region, the orientation preference of the upper part is {111}, which corresponds to TiN (111) planes. However, the film orientation close to the interface is {100}, which corresponds to TiN (200) planes. Preferred orientation switched from (200) to (111) in the middle of the film thickness. Moreover, considering the previous report, the preferred orientation of the film switches from (200) to (111) with film thickness [35]. These experimental evidences indicate that the middle of the film thickness is the film texture transition zone, which has a mixed texture.

3.6. Energy calculations

Petrov et al. [36] reported microstructure evolution as a function of the reduced temperature T_s/T_m, where T_s is the deposition temperature and T_m is the melting point of the material. As reported, the primary feature of the zone T type was competitive growth, which leads to a continuous change in morphology and texture as a function of film thickness. The TiN thin film in this work has zone type T characteristics. At the initial stage of film growth, the preferred orientation of the thin film in this work is (200) with lower surface energy. With the film growth continues to a certain degree, the (111) plane with higher surface energy becomes dominate [36].

The growth of thin film material is an energy-controlled process. The dominant orientation during film growth depends on the lowest energy state, which is derived from the interactions between the surface energy and the strain energy [37]. According to Fig. 7, the grain size is relatively small at early stages of film growth and gets larger with the film thickness. With the grain size increase, the porosity of the film reduces. Therefore, the grain boundaries density (length per surface area) gets lower for larger grain size. Lower grain boundaries density means less possibility to insert impurities or extra atoms into the grain boundaries. Impurities can alter the surface energy of different crystal planes [38]. At the early stages of film growth, surface energy is the dominant factor for preferred orientation, since the strain energy is negligible [39]. However, strain energy increases with the film growth. Once the film thickness reaches the critical value, the dominant factor for the preferred orientation will be strain energy rather than surface energy.

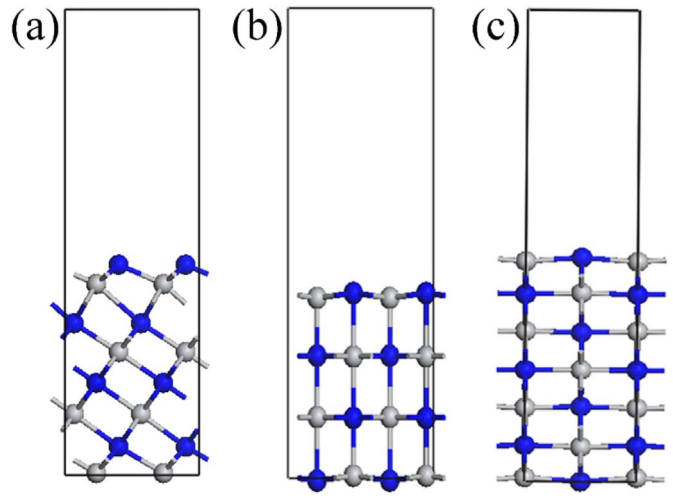

Fig. 7. Simulated structure of (a) TiN(111), (b) TiN(200) and (c) TiN(220) surface slabs. The gray and blue balls represent the Ti and N atoms, respectively.

From the thermodynamics viewpoint, the basic reason for forming the film structure is system free energy (ΔG) during the film growth. ΔG value commonly consists of the surface energy, the strain energy and the interface energy [27]:

$$\Delta G = \Delta E_{\text{surface}} + \Delta E_{\text{strain}} \tag{3}$$

where $\Delta E_{\text{surface}}$ and ΔE_{strain} represent the surface energy and the strain energy between the two neighboring grains, respectively. The surface energy was determined as in [28]:

$$E_{surface}^{hkl} = \frac{E_{slab}^{hkl} - \frac{N_{slab}^{hkl}}{N_{bulk}} E_{bulk}}{2A^{hkl}} \tag{4}$$

In this work, the surface energy of different film orientations was simulated based on the first principles calculations. These calculations were executed using the CASTEP module of Materials Studio 8.0 (Accelry Inc., USA). Generalized gradient approximation by the Perdew-Bruker-Ernzerhof method was used to calculate the exchange-correlation potential. During calculation, the cutoff energy was 350 eV, the total energy tolerance was 5×10^{-7} eV/atom, and the k-point was $10 \times 10 \times 1$. In the simulations, TiN (200) and TiN (111) surfaces were taken using the specific slabs with the lattice constant of 4.242 Å. The results are shown in Table 2. The 0.086 J m^{-2} surface energy of the (200) TiN orientation is the lowest among the three planes. The TiN (111) and TiN (220) orientations show higher surface energy of 0.209 J m^{-2} and 0.192 J m^{-2}, respectively. These results indicate that the surface energy minimization dominates the early stage growth with (200) TiN preferred orientation. The experimental findings of the film growth are in agreement with these results.

Table 2
Simulated and calculated values of the TiN thin films.

Plane	E_{bulk} (eV)	E_{slab}^{hkl}	A^{hkl} (10^{-20} m^2)	$E_{surface}^{hkl}$ (J·m^{-2})
TiN(111)	−7510.847	−30030.093	31.855	0.209
TiN(200)	−7510.847	−30037.343	35.144	0.086
TiN(220)	−7510.847	−18769.136	12.801	0.192

*1 eV = 1.602176565(35) × 10^{-19} J.

3.7. Film fracture toughness

Fracture toughness is crucial for failure problems. According to the simplified fracture model, the driving force for crack growth, G_c, can be obtained as follows [33]:

$$G_c = \frac{1-v_f^2}{2E_f}\sigma_m^2 h_{f1} + Uh_{f2} \tag{5}$$

where v_f, E_f and σ_m are the Poisson's ration, Young's modulus and the biaxial stress of the film, while h_{f1} and h_{f2} are the film thickness of the upper and lower layers in the fracture model proposed by Wang [33]. Besides, U represents the strain energy density of the lower part.

The total stored elastic energy, G_s, must be larger than G_c ($G_c > G_s$) to initiate the crack propagation. Under the assumption that all the film detached from the substrate, i.e. $h_{f2} = 0$, $h_{f1} = h_f$, one can get:

$$G_c = \frac{1-v_f^2}{2E_f}\sigma_m^2 h_f \tag{6}$$

According to the Griffith theory, the total energy is given as

$$E_{total} = -\frac{\sigma_m^2}{2E_f}wah_f + 2\gamma aw \tag{7}$$

where γ is the surface energy per unit area of the crack, w, a and h_f are the width and length of the crack and the film thickness, respectively.

The instability starts at $h_f = h_c$ when $\frac{dE_{total}}{da} = 0$, thus [33]:

$$\frac{dE_{total}}{da} = -\frac{\sigma_c^2}{2E_f}wh_c + 2\gamma w = 0 \tag{8}$$

Consequently, the critical stress is given by

$$\sigma_c = \sqrt{\frac{4E_f\gamma}{h_c}} \tag{9}$$

In Eq. (9), $\sqrt{4E_f\gamma}$ is usually referred to as K_{IC} [40], so one can get

$$K_{IC} = \sigma_c\sqrt{h_c} = \sqrt{4E_f\gamma} \tag{10}$$

Since residual stress originated from the two sources, growth and thermal, the thermal stress component should be assessed, and G_c can be expressed as in [33]:

$$G_c = \frac{1-v_f^2}{2E_f}\sigma_{XRD}^2 h_f + \frac{v_f^2}{2E_f}\sigma_{thermal}^2 h_f \tag{11}$$

where σ_{XRD} is the measured stress value of the thin film from X-ray diffraction method and $\sigma_{thermal}$ is the thermal stress. In Eq. (11), the effect of the thermal stress is the second term, $\frac{v_f^2}{2E_f}\sigma_{thermal}^2 h_f$. TiN thin films were deposited at 300 °C and cooled down to room temperature. By using the film thickness and elastic modulus of the TiN film in this study, the thermally-induced energy is less than 0.2 J/m^2, which is less than 1.2% of the fracture toughness from previous literature reports [33,41]. Therefore, it is reasonable to neglect the contribution of the thermal stress and K_{IC} can be expressed as [33]:

$$K_{IC} = \sigma_c\sqrt{h_c} = \sqrt{\frac{2E_f G_c}{1-v_f^2}} \tag{12}$$

It is reasonable to consider the fracture toughness as texture dependent since the preferred orientation is observed in the polycrystalline TiN thin films with film thickness. Moreover, Young's modulus is reported in some previous literature reports as a variable with preferred orientation of the thin films [42,43]. In Eq. (12), E_f' is used to substitute for E_f. Here, $E_f' = \alpha E_f$, and α is a coefficient that reflects the ratio of the modulus values of a specific plane to the mean value of the thin film. By inserting $v = 0.21$ [35] and eliminating the two dimensional geometry and biaxial stress state factor $\sqrt{2}$ [33], Eq. (12) can be converted to

Table 3
Fracture toughness and critical stress of different orientations of the TiN thin films.

Orientation	E (GPa)	α	K_{IC} (MPa $\sqrt{m}$)	σ_c (GPa)
(111) single-crystal	449 ± 28	1.45	2.75	1.38
(200) single-crystal	445 ± 38	1.44	2.74	1.37
(111) + (220) mixed texture	265 ± 11	0.86	2.12	1.06

$$K_{IC} = 1.0233\sqrt{\alpha E_f G_c} \tag{13}$$

Therefore, the fracture toughness of the film can be considered as texture dependent in Eq. (13). From the previous section, the mean Young's modulus value is 308.61 GPa. The elastic modulus of three main planes of the TiN films are given in [43]. Corresponding Young's modulus values, α values, fracture toughness and critical stress of different preferred orientations are listed in Table 3.

The reason for the film fracture behavior in Section 3.3 is due to the relatively low fracture toughness of the texture transition zone in the middle of TiN film cross-section compared to the surface and the interface. The fracture toughness of the film middle is 2.12 MPa $\sqrt{m}$, corresponding to the 1.06 GPa critical stress, which is obviously smaller than the film surface (1.38 GPa) and the interface (1.37 GPa) regions. This may lead to the crack initiation in the middle of the film thickness.

4. Conclusions

In this paper, in-situ film stress gradient evolution of thin hard magnetron sputtered TiN film was accurately characterized under externally applied load. The results indicate that the surface, the interface and the middle region of the film cross-section have different response when exposed to an intermediate applied strain ranging from 0.11% to 0.3%. The crack initiated in the middle of the film thickness, while the stress in the surface and the interface regions continued to increase. The crack then propagated into the surface and/or the interface areas with increased applied load. Eventually, film failed, inducing through-thickness cracks and even delamination.

Preferred orientation evolution along the film cross-section was confirmed by the SEAD TEM mode and the TKD of the film cross-section. The driving force of the transition was the energy minimization, which derived from the interaction between the surface energy and the strain energy. Thermodynamics modeling, based on the density functional theory, was conducted to show the surface energy different for several film orientations, which was responsible for the texture transition.

Fracture toughness difference of the various regions of the TiN film cross-sections accounts for the cracking behavior. The fracture toughness of the film is considered as texture-dependent. Moreover, a model of determining fracture toughness is proposed to take the effect of the preferred orientation into account. The model illustrated that the fracture toughness of the middle of the film thickness is smaller than the surface or the interface. As a result, the texture transition zone of the film becomes the more vulnerable place for crack initiation and finally leads to the failure of the whole film-substrate system.

Acknowledgements

This work was supported by the Beijing Nova Program (Z171100001117075), the National Natural Science Foundation of China (51771025), and the Fundamental Research Funds for the Central Universities (FRF-TP-17-002C1). The author would also like to thank Haijiao Xie from Shiyanjia lab for the support of the materials characterization.

References

[1] Y. Xi, S. Zhang, Toward hard yet tough ceramic coatings, Surf. Coat. Technol. 258 (2014) 1–16.
[2] M. Bartosik, M. Arndt, R. Rachbauer, C. Krywka, C.M. Koller, J. Keckes, P.H. Mayrhofer, Cross-sectional X-ray nano-diffraction and -reflectivity analysis of multilayered AlTiN–TiSiN thin films: correlation between residual strain and bi-layer period, Scr. Mater. 107 (2015) 153–156.
[3] Y. Chang, W. Chiu, J. Hung, Mechanical properties and high temperature oxidation of CrAlSiN / TiVN hard coatings synthesized by cathodic arc evaporation, Surf. Coat. Technol. 303 (2016) 18–24.
[4] G.S. Fox-rabinovich, J.L. Endrino, B.D. Beake, M.H. Aguirre, S.C. Veldhuis, Effect of temperature of annealing below 900 °C on structure , properties and tool life of an AlTiN coating under various cutting conditions, Surf. Coat. Technol. 202 (2008) 2985–2992.
[5] Xigui Sun, Kewei Gao, Xiaolu Pang, Huisheng Yang, Interface and strain energy revolution texture map to predict structure and optical properties of sputtered PbSe thin films, ACS Appl. Mater. Interfaces 8 (2016) 625–633.
[6] A. Karimi, Y. Wang, T. Cselle, M. Morstein, Fracture mechanisms in nanoscale layered hard thin films, Thin Solid Films 420–421 (2002) 275–280.
[7] S. Faulhaber, C. Mercer, M. Moon, Buckling delamination in compressed multi-layers on curved substrates with accompanying ridge cracks, J. Mech. Phys. Solids 54 (2006) 1004–1028.
[8] S. Lamri, C. Langlade, G. Kermouche, Damage phenomena of thin hard coatings submitted to repeated impacts: influence of the substrate and film properties, Mater. Sci. Eng. A 560 (2013) 296–305.
[9] R. Hahn, M. Bartosik, R. Soler, C. Kirchlechner, G. Dehm, P.H. Mayrhofer, Superlattice effect for enhanced fracture toughness of hard coatings, Scr. Mater. 124 (2016) 67–70.
[10] M. Tkadletz, N. Schalk, R. Daniel, J. Keckes, C. Czettl, C. Mitterer, Advanced characterization methods for wear resistant hard coatings: a review on recent progress, Surf. Coat. Technol. 285 (2016) 31–46.
[11] Y.C. Huang, S.Y. Chang, C.H. Chang, Effect of residual stresses on mechanical properties and interface adhesion strength of SiN thin films, Thin Solid Films 517 (2009) 4857–4861.
[12] R. Daniel, K.J. Martinschitz, J. Keckes, C. Mitterer, The origin of stresses in magnetron-sputtered thin films with zone T structures, Acta Mater. 58 (2010) 2621–2633.
[13] A.-N. Wang, J.-H. Huang, H.-W. Hsiao, G.-P. Yu, H. Chen, Residual stress measurement on TiN thin films by combing nanoindentation and average X-ray strain (AXS) method, Surf. Coat. Technol. 280 (2015) 43–49.
[14] M. Tkadletz, J. Keckes, N. Schalk, I. Krajinovic, M. Burghammer, C. Czettl, C. Mitterer, Residual stress gradients in α-Al_2O_3 hard coatings determined by pencil-beam X-ray nanodiffraction: the influence of blasting media, Surf. Coat. Technol. 262 (2015) 134–140.
[15] R. Ali, M. Sebastiani, E. Bemporad, Influence of Ti–TiN multilayer PVD-coatings design on residual stresses and adhesion, Mater. Des. 75 (2015) 47–56.
[16] M. Renzelli, M.Z. Mughal, M. Sebastiani, E. Bemporad, Design,fabrication and characterization of multilayer Cr-CrN thin coatings with tailored residual stress pro files, Mater. Des. 112 (2016) 162–171.
[17] R. Machunze, G.C. a.M. Janssen, Stress gradients in titanium nitride thin films, Surf. Coat. Technol. 203 (2008) 550–553.
[18] R. Daniel, M. Meindlhumer, W. Baumegger, J. Zalesak, B. Sartory, M. Burghammer, C. Mitterer, J. Keckes, Grain boundary design of thin films: using tilted brittle interfaces for multiple crack deflection toughening, Acta Mater. 122 (2017) 130–137.
[19] Z. Xia, W.A. Curtin, B.W. Sheldon, A new method to evaluate the fracture toughness of thin films, Acta Mater. 52 (2004) 3507–3517.
[20] S. Zhang, D. Sun, Y. Fu, H. Du, Toughness measurement of thin films: a critical review, Surf. Coat. Technol. 198 (2005) 74–84.
[21] X. Li, D. Diao, B. Bhushan, Fracture mechanisms of thin amorphous carbon films in nanoindentation, Acta Mater. 45 (1997) 4453–4461.
[22] J. Malzbender, J.M.J. den Toonder, A.R. Balkenende, G. de With, Measuring mechanical properties of coatings: a methodology applied to nano-particle-filled sol–gel coatings on glass, Mater. Sci. Eng. R Rep. 36 (2002) 47–103.
[23] C. Wang, J.M. Pureza, Y. Yang, Y.W. Chung, Investigation of hardness and fracture toughness properties of Fe/VC multilayer coatings with coherent interfaces, Surf. Coat. Technol. 288 (2016) 179–184.
[24] S. Zhang, D. Sun, Y. Fu, H. Du, Toughening of hard nanostructural thin films: a critical review, Surf. Coat. Technol. 198 (2005) 2–8.
[25] S. Zhang, X. Zhang, Toughness evaluation of hard coatings and thin films, Thin Solid Films 520 (2012) 2375–2389.
[26] J. Malzbender, G. De With, Energy dissipation, fracture toughness and the indentation load-displacement curve of coated materials, Surf. Coat. Technol. 135 (2000) 60–68.
[27] X. Li, B. Bhushan, Measurement of fracture toughness of ultra-thin amorphous carbon films, Thin Solid Films 315 (1998) 214–221.
[28] B. Bhushan, Chemical, mechanical and tribological characterization of ultra-thin and hard amorphous carbon coatings as thin as 3.5 nm: recent developments, Diam. Relat. Mater. 8 (1999) 1985–2015.
[29] R. Saha, W.D. Nix, Effects of the substrate on the determination of thin film mechanical properties by nanoindentation, Acta Mater. 50 (2002) 23–38.
[30] P.F. Tortorelli, K.L. More, E.D. Specht, B.A. Pint, Growth stress – microstructure relationships for alumina scales, Mater. High Temp. 20 (2003) 303–310.
[31] C.H. Ma, J.H. Huang, H. Chen, Residual stress measurement in textured thin film by grazing-incidence X-ray diffraction, Thin Solid Films 418 (2002) 73–78.
[32] J. Peng, V. Ji, W. Seiler, A. Tomescu, A. Levesque, A. Bouteville, Residual stress gradient analysis by the GIXRD method on CVD tantalum thin films, Surf. Coat. Technol. 200 (2006) 2738–2743.
[33] A. Wang, G. Yu, J. Huang, Fracture toughness measurement on TiN hard coatings using internal energy induced cracking, Surf. Coat. Technol. 239 (2014) 20–27.
[34] J.M. Cairney, S.G. Harris, P.R. Munroe, E.D. Doyle, Transmission electron microscopy of TiN and TiAlN thin films using specimens prepared by focused ion beam milling, Surf. Coat. Technol. 183 (2004) 239–246.
[35] Y. Xi, K. Gao, X. Pang, H. Yang, X. Xiong, Film thickness effect on texture and residual stress sign transition in sputtered TiN thin films, Ceram. Int. 43 (2017) 11992–11997.
[36] I. Petrov, P.B. Barna, L. Hultman, J.E. Greene, Microstructural evolution during film growth, J. Vac. Sci. Technol. A 21 (2003) S117.
[37] D. Dinesh Kumar, N. Kumar, S. Kalaiselvam, S. Dash, R. Jayavel, Substrate effect on wear resistant transition metal nitride hard coatings: microstructure and tribo-mechanical properties, Ceram. Int. 41 (2015) 9849–9861.
[38] M. Adamik, P. Barna, I. Tomov, Columnar structures in polycrystalline thin films developed by competitive growth, Thin Solid Films 317 (1998) 64–68.
[39] U.C. Oh, J.H. Je, Effects of strain energy on the preferred orientation of TiN thin films, J. Appl. Phys. 74 (1993) 1692–1696.
[40] M. Ohring, Materials Science of the Thin Film: Deposition and Structure, Academic Press, 2002, p. 762.
[41] S. Zhang, D. Sun, Y. Fu, H. Du, Toughness measurement of ceramic thin films by two-step uniaxial tensile method, Thin Solid Films 469–470 (2004) 233–238.
[42] J.E.S.H. Ljungcrantz, M. Oden, L. Hultman, J.E. Greene, Nanoindentation studies of single-crystal (001)-, (011)-, and (111)-oriented TiN layers on MgO, J. Appl. Phys. 80 (1996).
[43] G. Abadias, S. Dub, R. Shmegera, Nanoindentation hardness and structure of ion beam sputtered TiN, W and TiN/W multilayer hard coatings, Surf. Coat. Technol. 200 (2006) 6538–6543.